HAL
open science

Simultaneous photocatalytic Cr(VI) reduction and phenol degradation over copper sulphide-reduced graphene oxide nanocomposite under visible light irradiation: Performance and reaction mechanism

Yacine Cherifi, Alexandre Barras, Ahmed Addad, Baghdad Ouddane, Pascal Roussel, Ahcène Chaouchi, Sabine Szunerits, Rabah Boukherroub

To cite this version:

Yacine Cherifi, Alexandre Barras, Ahmed Addad, Baghdad Ouddane, Pascal Roussel, et al.. Simultaneous photocatalytic Cr(VI) reduction and phenol degradation over copper sulphide-reduced graphene oxide nanocomposite under visible light irradiation: Performance and reaction mechanism. Chemosphere, 2021, pp.128798. 10.1016/j.chemosphere.2020.128798 . hal-03089826

HAL Id: hal-03089826

https://hal.science/hal-03089826v1

Submitted on 23 Aug 2021

HAL is a multi-disciplinary open access archive for the deposit and dissemination of scientific research documents, whether they are published or not. The documents may come from teaching and research institutions in France or abroad, or from public or private research centers.

L'archive ouverte pluridisciplinaire **HAL**, est destinée au dépôt et à la diffusion de documents scientifiques de niveau recherche, publiés ou non, émanant des établissements d'enseignement et de recherche français ou étrangers, des laboratoires publics ou privés.

Simultaneous photocatalytic Cr(VI) reduction and phenol degradation over copper sulphide-reduced graphene oxide nanocomposite under visible light irradiation: Performance and reaction mechanism

Yacine Cherifi,[1,2] Alexandre Barras,[1] Ahmed Addad,[3] Baghdad Ouddane,[4] Pascal Roussel,[5] Ahcène Chaouchi,[2] Sabine Szunerits,[1] Rabah Boukherroub[1*]

[1]*Univ. Lille, CNRS, Centrale Lille, Univ. Polytechnique Hauts-de-France, UMR 8520 - IEMN, F-59000 Lille, France*

[2]*Laboratoire de Chimie Appliquée et Génie Chimique de l'Université Mouloud Mammeri de Tizi-Ouzou, Algérie*

[3]*Univ. Lille, CNRS, UMR 8207 – UMET, F-59000 Lille, France*

[4]*Univ. Lille, UMR CNRS 8516 - LASIRE Laboratoire Avancé de Spectroscopie pour les Interactions, la Réactivité et l'Environnement, F-59655 Villeneuve d'Ascq, France*

[5]*Univ. Lille, CNRS, ENSCL, Centrale Lille, Univ. Artois, UMR8181, UCCS-Unité de Catalyse et Chimie du Solide, Lille, F-59000, France*

*To whom correspondence should be addressed: rabah.boukherroub@univ-lille.fr

Abstract

The contamination of water by synthetic organic molecules and trace metals is a growing challenge, in spite of the enormous research efforts being made in the field of water treatment. In this study, reduced graphene oxide-copper sulphide (rGO-CuS) nanocomposites of different rGO/CuS (2/1, 1/1, 1/2) molar ratios were fabricated *via* a facile one-step hydrothermal method. The nanocomposite materials, named hereafter as 2rGO-CuS, rGO-CuS and rGO-2CuS, were characterized using various analytical techniques, including X-ray diffraction (XRD), Raman spectroscopy, transmission electron microscopy (TEM), energy dispersive X-ray (EDX) spectroscopy, X-ray photoelectron spectroscopy (XPS) and UV–visible spectrophotometry. The photocatalytic performance of the nanocomposites was assessed under visible light irradiation ($\lambda > 420$ nm) for the simultaneous photocatalytic reduction of Cr(VI) and phenol degradation. It was found that rGO-2CuS achieved a remarkable enhancement of the photocatalytic activity among the prepared nanocomposites for the degradation of phenol and reduction of Cr(VI). Therefore, the simultaneous photocatalytic phenol degradation and Cr(VI) reduction over rGO-2CuS sample was further investigated. The experimental results revealed that rGO-2CuS catalyst maintained good degradation efficacy of mixed pollutants after 6 runs and dissolved oxygen was found to be essential to promote Cr(VI) reduction and phenol degradation. A detailed photocatalytic activity under visible light irradiation mechanism was proposed based on quenching experiments and fluorescence measurements.

Keywords: rGO/CuS nanocomposites; Photocatalysis; Phenol degradation; Cr(VI) removal.

1. Introduction

Photocatalysts are nowadays increasingly used to treat environmental problems, in particular excessive discharges of industrial waste water. Industrial wastewater is often loaded with traces of toxic metal ions (e.g., Cr(VI), Cd(II), As(V)), Hg(II)) as well as with harmful organic pollutants (e.g., organic dyes, polychlorinated biphenyls, phenol…) at the same time [1-3]. Among the metal ions, hexavalent chromium, Cr(VI), is a highly toxic and non-biodegradable pollutant, which can cause different health problems such as cancer pulmonary congestions, and liver damage. Owing to its high toxicity, Cr(VI) has been classified as a priority pollutant by the United States Environmental Protection Agency (USEPA) and many other countries [4, 5]. Therefore, several methods have been developed for Cr(VI) removal, including ion exchange, chemical precipitation, adsorption and membrane separation techniques [6, 7]. Currently, the reduction of Cr(VI) to Cr(III) using photocatalysis is considered to be the most promising approach, as it reduces the highly toxic Cr(VI) to less harmful Cr(III), a trace element necessary for human beings [8]. On the other hand, organic pollutants like phenolic compounds are major pollutants of the aquatic environment with carcinogenic and mutagenic characters, causing a risk to human health [9, 10].

Hence, the development of catalysts for the simultaneous removal of organic pollutants and metal ions from wastewater represents an appealing approach. The strategy consists of using semiconductor catalysts, which upon light irradiation, the photogenerated electron-hole pairs are consumed separately in the corresponding oxidation and reduction half-reactions. This process not only prevents the recombination of the electron-hole pairs, but also improves the photocatalytic efficiency [11, 12].

Although semiconductors such TiO_2, ZnO and their nanocomposites have been used for the simultaneous Cr(VI) reduction and phenol oxidation [11, 13-15], these photocatalytic processes have been conducted under UV light irradiation due to the wide band gaps of TiO_2 and ZnO,

which hinders their widespread application. To overcome this limitation and extend photocatalyst absorption to the visible range, coupling TiO_2 with other semiconductor materials has been adopted as an effective strategy. For instance, TiO_2/Co-g-C_3N_4 [16], Tb_xO_y loaded TiO_2-oriented nanosheets [17], N-doped TiO_2-carbon composite fibres [18], Cu-doped TiO_2 nanoparticles modified with 8-hydroxyquinoline [19], carbon nitride loaded into titanium incorporated SBA-15 mesoporous silica (Ti-SBA15-CN) [10], and CdS/TiO_2 [20] have been successfully applied for simultaneous removal of metal ions and organic pollutants. For a more efficient use of visible light, various narrow-band gap semiconductor photocatalysts, such as $BiVO_4$ [21], bismuth oxyiodide/reduced graphene oxide/bismuth sulphide (BiOI/rGO/Bi_2S_3) [22], PANI-sensitized g-C_3N_4/$ZnFe_2O_4$ heterostructure [23], AgI(β)/Bi_2O_3(β)- $Bi_2O_2CO_3$ composite [24], and Au-Pd nanoparticles loaded on g-C_3N_4/MCM-41 [25] have been investigated for this photochemical process. Nevertheless, it is well-established that some of these photocatalysts have certain disadvantages such as photo-corrosion and instability. Therefore, it is important to develop highly efficient and robust photocatalysts for the simultaneous treatment of mixed pollutants.

A huge effort has been devoted to the development of visible light photocatalysts to maximize the use of clean, safe and abundant solar energy. In recent years, transition metal dichalcogenide (TMD) nanostructures have drawn enormous attention, owing to their outstanding electronic and optical properties as well as their wide applications in different fields, including energy conversion devices, photocatalysis, photovoltaics, biosensors, etc. [26-28]. Among them, the non-toxic, cheap and *p*-type semiconductor copper sulphide (CuS) exhibits excellent luminescence and photochemical properties with a narrow band gap (1.2–2.2 eV), which is dependent on the CuS crystalline phase. CuS can harvest efficiently photons in the visible absorption window and thus makes it an interesting semiconductor for photocatalytic processes [2, 29]. However, the catalytic activity of CuS is not satisfactory due

to its poor absorption and low separation efficiency of photogenerated electron-hole pairs along with its anti-photo-corrosion stability. Therefore, improving the photo-activity and photostability of CuS remains a challenge and a priority for practical application in the environmental field [30, 31].

Graphene-based materials have received a great deal of attention. Currently, constructing heterostructures between semiconductors and graphene can reduce the possibility of electron-hole pair recombination to further improve the photocatalytic performance [32, 33]. Due to the presence of electronic interactions and the charge equilibrium between semiconductor materials and graphene sheets, the potential of the conduction band of the materials is reduced, resulting in an increase in the photoinduced electron migration efficiency and a negative shift in the Fermi level of the materials [34, 35]. In addition, graphene acting as a carrier could enhance the degree of dispersion of the original samples to provide more reactive sites, which would lead to increased photocatalytic activity [34].

In the present study, we report a facile and practical strategy for the synthesis of reduced graphene oxide-copper sulphide (rGO-CuS) composites by a one-step hydrothermal approach. Their catalytic activities are systematically investigated for the simultaneous photocatalytic reduction of Cr(VI) and oxidation of phenol to seek enhanced performance. In order to better understand the synergistic effect between Cr(VI) reduction and oxidation of phenol, systematic experiments were performed, including control experiments to reveal the roles of Cr(VI), phenol and rGO-CuS in the oxidation and reduction processes. The effects of the initial concentration of the substrates, pH and active oxygen species in the degradation process were investigated experimentally and the photocatalytic degradation mechanism was therefore proposed.

2. Experimental section

2.1. Synthesis of catalysts

The preparation of the rGO-CuS nanocomposites (2rGO-CuS, rGO-CuS and rGO-2CuS) was carried out by an easy hydrothermal method in a one-step process. To 40 mL of Milli-Q (MQ) water was added 40 mg of graphene oxide (GO) powder. A homogeneous solution was prepared by ultrasonic (464 W, 35 Hz) irradiation for 2 h. To this solution was added 20, 40 or 80 mg of copper sulphate ($CuSO_4$) under magnetic stirring to obtain a solution (a). Then 25 mg of thiourea was dissolved in 25 mL of MQ water to obtain a solution (b). Solutions (a) and (b) were mixed together and transferred into a 100 mL Teflon-lined autoclave and heated at 110 °C for 14 h. The suspensions of the obtained mixtures 2rGO-CuS, rGO-CuS and rGO-2CuS were centrifuged at 8000 rpm for 20 min for efficient separation from supernatant, washed repeatedly with MQ water and ethanol, and finally dried in a vacuum oven at room temperature for 12 h. For comparison, the pure CuS was synthesized by the similar experimental process in absence of GO powder. Similarly, rGO was prepared in absence of CuS precursors under the same hydrothermal process.

2.2. Photocatalytic activity test

The photocatalytic activities of the products were tested for the reduction of Cr(VI) under visible light irradiation. For all photocatalytic tests, a 50 mL aqueous solution containing a certain amount of Cr(VI) ($K_2Cr_2O_7$) and 0.5 g L^{-1} of the catalyst in absence or presence of phenol was prepared. The pH of the suspension was adjusted by using 0.1 M HCl or 0.1 M NaOH solution. The resulting suspension was ultrasonicated for 1 min and magnetically stirred for 0.5 h in the dark to ensure adsorption–desorption equilibrium.

The aqueous solution was irradiated under stirring at room temperature in air through with a cut off filter ($\lambda > 420$ nm, to suppress the light with wavelength shorter than 420 nm) using a visible fiber lamp (Spot Light Source 400–700 nm, L9566-03, Hamamatsu, Japan). The

150 intensity of the light was measured using a PM600TM Laser Fiber Power Meter (Coherent Inc,
151 USA) and was determined as being 0.4 W cm^{-2}. During the visible light irradiation, about 2 mL
152 of the suspension was taken from the reaction cell at given time intervals, and then centrifuged
153 to remove the photocatalyst particles. The concentration of Cr(VI) was determined by the
154 diphenylcarbazide (DPC) method [15]. The absorbance of sample solutions was measured
155 using UV–vis spectrophotometry at 540 nm after full color development. The concentration of
156 phenol was measured by a HPLC system. Additionally, the total Cr content was also determined
157 by ICP-AES.

158 **2.3. Hydroxyl radical ($^{\bullet}OH$) formation measurement**

159 The formation of $^{\bullet}OH$ radicals in presence of rGO, CuS, 2rGO-CuS, rGO-CuS and rGO-2CuS
160 under visible light illumination was monitored by using terephthalic acid (TA) as the
161 fluorescence probe. It is known that TA reacts with $^{\bullet}OH$ in basic solution to generate 2-
162 hydroxylterephthalic acid (TAOH), which fluoresces at approximately 426 nm upon excitation
163 at 312 nm [36]. In a typical process, 0.5 g/L of nanocomposite were dispersed in an aqueous
164 solution (3 mL) containing 5×10^{-4} M TA and 2×10^{-3} M NaOH in a spectrometric quartz
165 cuvette. The mixed solution was stirred in the dark for 10 min. After irradiation under the visible
166 light, the reaction solution was centrifuged to remove the sample particles. The filtrate was
167 analyzed using a PL spectrophotometer.

168

169 **3. Results and discussion**

170 **3.1. Characterization**

171 The phase composition and crystal structure of the CuS and CuS-rGO nanocomposites were
172 studied with X-ray diffraction (XRD) (**Fig. 1** and **Fig. S1)**. The presence of sharp diffraction
173 peaks evidences that the as-obtained products are crystalline. The XRD patterns of CuS and
174 CuS-rGO nanocomposites comprise several peaks at 10.8°, 21.7°, 27.1°, 27.6°, 29.2°, 31.7°,

175 32.7°, 38.8°, 43.2°, 44.3°, 47.8°, 52.7°, 57.1° and 59.3° ascribed to the (002), (004), (100),
176 (101), (102), (103), (006), (105), (106), (008), (110), (108), (202) and (116) diffraction planes,
177 respectively [37]. All the diffraction peaks can be perfectly indexed as hexagonal covellite CuS
178 (space group: P63|*mmc*), which are in good agreement with the JCPDS no. 78-2391, with cell
179 parameters a=3.796 Å and c=16.36 Å. The absence of GO diffraction peak and the appearance
180 of broad diffraction peak at ~22.4° in the XRD patterns of CuS-rGO nanocomposites indicates
181 the effective reduction of GO to rGO [38]. The XRD patterns reveal that the products were
182 devoid of any detectable impurities or any other phases. Moreover, the addition of GO did not
183 affect the crystal orientation of the CuS nanocomposites.

184 Raman spectroscopy is a powerful and non-destructive technique for investigating the
185 structural nature of carbon-based materials such as graphene [39, 40]. **Figure S2** depicts the
186 Raman spectra of GO, rGO, CuS and rGO-CuS nanocomposites. The Raman spectrum of GO
187 exhibits two main characteristic peaks, the D band at ~1368 cm^{-1} attributed to defects and
188 disorder in the hexagonal graphitic layers, and the G band at ~1589 cm^{-1} ascribed to the
189 vibration of sp^2 carbon atoms in the 2D hexagonal lattice. Similarly, the Raman spectrum of
190 rGO comprises the characteristic D and G bands at respectively 1368 and 1589 cm^{-1}.
191 Meanwhile, the Raman spectrum of the CuS displays a strong and sharp band at ~468 cm^{-1}
192 assigned to the S-S stretching mode of A_{1g} symmetry of CuS with a hexagonal structure [41,
193 42]. For rGO-CuS nanocomposites, all the Raman spectra consist of the D and G bands of rGO
194 along with the peak of CuS. It is important to notice a red-shift of the D and G bands to 1353
195 and 1584 cm^{-1}, respectively, indicating the high ability for recovery of the hexagonal network
196 of carbon atom and the presence of charge transfer between rGO and CuS [42].

197 The intensity ratio of the D and G bands (I_D/I_G) for rGO-2CuS increases to 1.31 (**Table S1**), as
198 compared to 0.85 recorded for GO. These observations further confirm the formation of new

199 and smaller sp^2 domains and testifies the reduction of GO to rGO during the hydrothermal
200 reaction [40]. The results are in good agreement with XRD patterns.

201 Transmission electron microscopy (TEM) and selected area electron diffraction (SAED)
202 were further performed to assess the mesoporous structure and morphology of CuS and rGO-
203 2CuS nanocomposite. **Figure 2a** depicts the TEM image of rGO-2CuS nanocomposite. It can
204 be seen that all rGO sheets are densely decorated with a large quantity of small nanoparticles,
205 and the rGO sheets in the composite are made of a few layers of graphene sheets. A close look
206 at these nanoparticles reveals that they are randomly distributed on the surface with size ranging
207 from 20 to 30 nm, as shown in **Figure 2c**. The HRTEM image, conducted on the scattered
208 nanosheets, is displayed in **Figure 2b**. The regular spacing of the clear lattice planes is
209 calculated to be 0.305 nm, which is consistent with the d spacing for the (1 0 2) crystal plane of
210 hexagonal phase of CuS [2]. Furthermore, the selected area electron diffraction (SAED) pattern
211 demonstrated the growth of single crystals of CuS **(Fig. 2d)**. Thus, these results are in good
212 agreement with XRD analysis.

213 In addition, the corresponding EDX plot is shown in **Figure S3**. It clearly confirms the
214 presence of Cu, S, and C elements with an atomic ratio of elemental copper and sulfur of
215 approximately 1:1 (other peaks originate from the substrate used). This result indicates that
216 individual CuS nanoparticles are well anchored onto the graphene sheets during the
217 hydrothermal synthesis and prevent the restacking of rGO sheets during the reduction process.

218 The chemical composition of the rGO-2CuS composite was further confirmed by X-ray
219 photoelectron spectroscopy (XPS) analysis (**Fig. S4**). The XPS survey spectrum in **Figure S4a**
220 clearly shows the peaks of Cu_{2p}, S_{2p}, O_{1s}, and C_{1s} [2, 42]. The O_{1s} and C_{1s} originate from rGO.
221 **Figure S4b** displays the core level spectrum of the Cu_{2p}, comprising two peaks at 933.75 and
222 953.54 eV, which can be appropriately curve-fitted with four bands. The peaks at 933.75 and
223 952.25 eV are assigned respectively to $Cu_{2p3/2}$ and $Cu_{2p1/2}$ of Cu^+, while the peaks at 935.75 and

954.38 eV are attributed to the characteristic peaks of $Cu_{2p3/2}$ and $Cu_{2p1/2}$ of Cu^{2+}, in accordance with the literature data [43]. The Auger line of Cu (Cu LMM) at 568.4 eV is the typical binding energy value of CuS [42, 44]. Also, the two weak shake-up satellite lines at 943.0 eV and 962.6 eV indicate the presence of the paramagnetic chemical state of Cu^{2+} [2, 42, 44]. In the case of S_{2p} region (**Fig. S4c**), the deconvolution of the S_{2p} spectrum leads to two main doublets at (161.5, 163.8 eV) and (164.6, 165.4 eV), that are typical values for metal sulphides and can be attributed to sulphide and disulphide, respectively [43]. Moreover, the peaks at (166.4, 168.13 eV) and (168.97, 170.11 eV) are assigned to polysulfides, sulfate or thiosulfate (SO_4^{2-} or $S_2O_3^{2-}$) due to some surface oxidation [43]. The core level C_{1s} spectrum of the rGO-2CuS composite can be curve-fitted with three Gaussian peaks (**Fig. S4d**). The peak centered at 284.4 eV is attributed to the conjugated sp^2-type C=C bonding in graphitic structure and the other two peaks located at 285.0 and 288.7 eV are ascribed to C-C and C=O, respectively [39, 45]. Overall, the XPS data suggest that rGO-2CuS is well formed.

Figure S5a displays the UV–vis absorption spectra of the synthesized rGO, CuS and CuS-rGO composites dispersed in water. The rGO exhibits an absorption peak at 245 nm, which can be assigned to the π-π* transition of aromatic C-C bonds along with a band at 410 nm due to the n-π* transition of C=O bonds [39]. The UV–vis absorption spectrum of pure CuS displays a characteristic covellite CuS-like absorption band in the near-IR region due to inter-band transitions between valence and unoccupied states [2, 42, 45]. The strong absorption in the visible range holds promise for the potential application of CuS-based materials in photocatalytic processes. Following the introduction of rGO, the absorbance of rGO-CuS composites increased throughout the spectrum compared to the CuS sample as a result of the absorption effect of rGO and the quantum effect of CuS. Moreover, it can be seen that a larger blue absorption profile has occurred, which might be attributed to quantum confinement [46].

248 The optical band gap was calculated using Eq. (1) by plotting $(\alpha h\upsilon)^2$ *vs.* $(\alpha\upsilon)$, where 'α' is the
249 absorption coefficient, 'hυ' is the photon energy, 'A' is a constant, 'E_g' is the band gap and 'n'
250 depends on the type of band gap of the semiconductor (for a direct gap, n = 1/2, while for an
251 indirect band gap, n = 2).

$$(\alpha h\upsilon)^n = A\left(\alpha\upsilon - E_g\right) \quad (1)$$

252
253 A plot of $(\alpha h\upsilon)^2$ *vs.* (hυ) gives a line whose interception on the energy axis corresponds to the
254 energy band gap. According to the above equation and based on a direct transition, as shown in
255 **Fig. S5b**, the calculated optical band gap of pure CuS was 2.13 eV. Upon hybridization with
256 rGO, the optical band gap of rGO-CuS nanocomposites changed from 2.06 to 1.96 eV when
257 GO content increased from 1 to 2. These band gaps are higher than the bulk value, which could
258 be due to quantum confinement in the small crystalline CuS nanostructures.

259 **3.2. Photocatalytic performance**

260 **3.2.1. Photocatalytic reduction of Cr(VI)**

261 The photocatalytic performance of the rGO-CuS nanocomposites (0.5 g/L) was examined
262 for the reduction of Cr(VI) (20 mg/L) aqueous solution as a toxic heavy metal pollutant. As
263 shown in **Figure 3**, no reduction occurred in absence of light or photocatalyst alone, indicating
264 that the reaction was mainly due to photocatalysis. The slight decrease of the Cr(VI) absorption
265 (~15%) after 30 min in the dark was ascribed to metal ion adsorption on the catalyst surface.

266 Under visible-light irradiation, rGO alone achieved a very weak performance for the
267 photocatalytic Cr(VI) reduction. CuS revealed high photoreduction activity of Cr(VI) to Cr(III)
268 with complete reduction after 70 min. Interestingly, the performance of CuS for Cr(VI)
269 photoreduction was improved through hybridization with rGO. Indeed, it could be seen that the
270 time for the complete reaction was reduced to 60 and 50 min in the presence of rGO-CuS and
271 rGO-2CuS, respectively. This contrasts with 2rGO-CuS catalyst for which a decrease of the

272 photocatalytic activity was observed (80% reduction after 70 min, as compared to 100%
273 achieved by CuS alone under otherwise identical experimental conditions). This decreased
274 activity can be ascribed to the reduced amount of CuS within 2rGO-CuS. All together, these
275 findings suggest that the visible light-induced photocatalytic activity of CuS nanoparticles can
276 be enhanced through hybridization with rGO, which is most likely due to increased efficiency
277 of light absorption and enhanced electron-hole separation of rGO-CuS nanocomposites [47].

278 **3.2.2. Effect of light intensity**

279 The influence of light intensity on Cr(VI) photoreduction process was investigated for light
280 intensity ranging from 0.1 to 0.5 W/cm^2 (**Fig. S6)**. It was found that the photoreduction kinetics
281 were significantly affected by the light intensity; decreasing of the light intensity from 0.4 to
282 0.1 W/cm^2 led to a clear decrease of the reduction rate from 100 to 85% after 70 min. In contrast,
283 increasing the light intensity to 0.5 W/cm^2 had no effect on Cr(VI) reduction rate. Therefore,
284 the optimal irradiation intensity of visible light was fixed at 0.4 W/cm^2.

285 **3.2.3. Effect of pH on photoreduction of Cr(VI)**

286 The pH of the solution is a critical parameter in the photocatalytic process. The reduction
287 of Cr(VI) at different initial pH values is summarized in **Figure S7**. The kinetic of Cr(VI)
288 photoreduction increased slightly after 50 min of visible light illumination upon decreasing the
289 initial pH value from 5.8 (the pH of the initial solution) to 2.5, whereas only 66.3% and 33.7%
290 of Cr(VI) were photocatalytically removed at pH 7 and 8.5 within the same period, respectively.
291 The effect of the acidified pH is consistent with the reported results [10, 15].

292 The dominant chromium species in the solution at pH 2.5 is $HCrO_4^-$ or $Cr_2O_7^{2-}$ [5, 10].
293 Under these conditions, the photocatalyst surface can be highly protonated and thus leads to a
294 strong electrostatic attraction towards the main species in solution. The pH could significantly
295 influence the reduction of Cr(VI) to Cr(III) and a decrease in pH could increase the reduction
296 kinetics of Cr(VI) [5, 48]. Moreover, Cr(III) could form $Cr(OH)_3$ which could precipitate on

297 the surface of the photocatalyst at high pH solution, covering the activity sites of the catalysts
298 [8, 48].

299 **3.2.4. Synergistic effect of phenol on Cr(VI) photoreduction**

300 It has been previously reported in the literature that the coexistence of metal-organic
301 pollutants may enhance the photocatalytic reduction of Cr(VI) [10, 49]. In this work, the
302 influence of variable initial phenol concentration on the reduction of 20 mg/L Cr(VI) over rGO-
303 2CuS (0.5 g/L) was investigated (**Fig. 4a**). In the presence of phenol, the complete
304 photoreduction time of Cr(VI) was reduced from 50 to 20 min when the Cr(VI)/phenol ratio
305 was increased to 1:2, suggesting that the presence of phenol could improve Cr(VI) removal by
306 acting as a scavenger of photo-generated holes. It can be seen that upon increasing the
307 Cr(VI)/phenol ratio to 1:3, the time required to reach full reduction of Cr(VI) increased. This is
308 maybe due to an increase in intermediates adsorbed on the rGO-2CuS nanocomposite surface
309 with the increase in phenol concentration, which could cover the active sites of the catalyst [15].

310 **3.2.5. Effect of Cr(VI) on phenol photodegradation**

311 To assess the influence of Cr(VI) on phenol degradation, an aqueous solution of phenol (20
312 g/L), rGO-2CuS (0.5 g/L) and Cr(VI) (10 g/L) was irradiated under visible light for different
313 time intervals. It could be observed that the extent of phenol degradation also increased greatly
314 until complete degradation after 20 min of irradiation, following the addition of phenol/Cr(VI)
315 (1:2), as shown in **Figure 4b**. Furthermore, the improvement of phenol degradation indicates
316 that Cr(VI) is an efficient scavenger of photo-generated electrons, which is similar to the
317 observation reported in the literature [50, 51]. The results confirmed the synergistic effect
318 between Cr(VI) reduction and phenol oxidation.

319 The performance of the developed photocatalyst is comparable to and even better than that
320 achieved by the most photocatalysts described in the literature for the simultaneous Cr(VI)
321 photoreduction and phenol degradation (**Table S2**).

3.2.6. Kinetic study

The modeling of the kinetic data with an appropriate kinetic model allows to determine the apparent rate constant and the order of reaction of the photocatalytic process. It is well-established that the rate (r) of a photocatalytic reaction for a single component can be defined using equation (2) [50, 52]:

$$r = ln\left(\frac{C}{C_0}\right) \approx -kKt = -k_{app} \quad (2)$$

where C_0 is the initial concentration, C is the concentration of reactant, t is time, k is the rate constant of reaction, and k_{app} is the apparent rate constant.

Although this pseudo first-order rate equation has been extensively used in the literature for modeling photocatalytic kinetic data, it is based on the Langmuir classical isothermal model, which assumes a homogeneous surface. However, the surface of a catalyst is rarely homogeneous and several studies have been carried out in this regard suggested the possibility to use modified Langmuir–Freundlich isotherm (an isotherm for adsorption onto heterogeneous surface from liquid phase), Equation 3 [52].

$$ln\left(\frac{C}{C_0}\right) = -k_{app}[cat]^{\alpha}t \quad (3)$$

where the plot of $\ln(C/C_0)$ *versus* t should give a line with a slope of $-k_{app}\,[cat]^{\alpha}$.

The determination of the order of reaction (α) is made by the methods introduced recently in refs. [52, 53]. By plotting the normalized concentration (C/C_0) *versus* normalized time scale (t $[cat]^{\alpha}$) at different concentrations of catalyst, the reaction order can be determined.

To study the kinetics of the photoreduction of Cr(VI) and phenol, the curves of $\ln(C/C_0)$ *vs.* time were plotted at different conditions (**Fig. S8**). All plots are linear, confirming the pseudo first-order reaction under the investigated experimental conditions. The obtained values of k_{app} are summarized in **Tables S3** and **S4**.

3.27. Analysis of by-products of Cr(VI) and phenol

In order to better understand the photocatalytic process, the total residual concentration of Cr ions after photocatalytic reduction was assessed by ICP-AES. The experiment was carried

350 out by visible light irradiation of a mixture of Cr(VI) (20 mg/L), phenol (20 mg/L) and GO-
351 2CuS (0.5 mg/L) at pH 5.8 (**Fig. 5**). After 20 min of irradiation, a concentration of 0.015 mg/L
352 of residual Cr(VI) ions was measured. This is far below the maximum allowable concentrations
353 of 0.25 mg/L for industrial wastewater and 0.05 mg/L for drinking water [1, 50, 54].

354 Furthermore, XPS analysis was used to study the chemical states of the Cr species adsorbed
355 on the catalyst surface after the photoreaction (**Fig. S9**). In the high-resolution spectrum of the
356 Cr_{2p}, the peaks located at 586.9 and 576.7 eV corresponding respectively to the 2p3/2 and 2p1/2
357 orbitals are attributed to Cr(III) [2, 55]. These results also confirm that rGO-2CuS
358 nanocomposite is not only capable of simultaneously reducing Cr(VI) and oxidizing phenol,
359 but also of removing Cr ions by adsorption [10, 15].

360 To investigate further the mechanism of phenol degradation using rGO-2CuS
361 nanocomposite, the generated intermediate products were identified using high-performance
362 liquid chromatography (HPLC). The results of HPLC (**Fig. S10**) revealed that two main
363 intermediates identified as hydroquinone (7.4 min) and 1,4-benzoquinone (10.9 min) were
364 formed. Their identification by HPLC was done based on their retention time, as compared to
365 standard chemicals (**Fig. S11**). These by-products are formed following $^{\bullet}OH$ radical addition to
366 the benzenic ring of phenol to yield hydroquinone and its subsequent oxidation to 1,4-
367 benzoquinone. It is not excluded that other by-products, derived from the ring-opening such as
368 short-chain acids, are also generated during the photochemical degradation of phenol over rGO-
369 2CuS [9]. However, the products derived from the opening of the benzene ring could not be
370 identified by HPLC. Instead, approximately 95% of the phenol was mineralized in 20 min (**Fig.
371 S12**), suggesting that the phenol was not only decomposed into small organic compounds, but
372 even mineralized into inorganic carbonaceous forms.

373 **3.2.8. Stability of rGO-2CuS photocatalyst**

374 Durability plays a key role in photocatalysis. Therefore, the repeatability and stability of the
375 photocatalyst were investigated. **Figures S13** and **S14** depict the performance of the recycled
376 rGO-2CuS nanocomposite for the mixed Cr(VI)/phenol system under visible light irradiation.
377 The photocatalyst was recovered by centrifugation after each cycle to regenerate the
378 photocatalyst and reused in the next cycle without any additional treatment. As can be observed,
379 even after 5 photocatalytic cycles, the photoreduction efficiency of Cr(VI) and phenol oxidation
380 were as high as 92% and 88%, respectively, and no significant loss of photocatalytic activity
381 can be seen during the cycling experiments. Furthermore, to demonstrate the stability of the
382 rGO-2CuS, XRD analysis of the used photocatalyst wa performed (data not shown). The results
383 revealed that no significant changes took place in the XRD patterns before and after the cycling
384 test, indicating that the catalyst exhibits good visible-light photocatalytic stability.

385 **3.2.9. Mechanism of the photocatalytic activity**

386 **Figure 6** displays the photocatalytic conversion rates of Cr(VI) and phenol over rGO-2CuO
387 in the presence of different radical scavengers under visible light (> 420 nm) irradiation for 20
388 min. For reaction under N_2 ambient conditions, before the start of the experiments, the reaction
389 solution was purged with high-purity N_2 (> 99.999%) for 1 h to remove dissolved O_2 as much
390 as possible, and continued to purge N_2 through the photocatalytic process. The recorded rates
391 of Cr(VI) reduction (**Fig. 6a**) and phenol degradation (**Fig. 6b**) in the mixed reaction system
392 were higher in ambient air than in ambient N_2. This could be due to the major role of O_2 in the
393 photocatalytic reaction process, through the reaction of dissolved O_2 with photogenerated
394 electrons to produce the $O_2^{\bullet-}$/$^{\bullet}$OOH superoxide radicals [8, 51]. In the case of Cr(VI) reduction,
395 the suppression effect was more evident, it is ca. 60% Cr(VI) reduction after 40 min irradiation
396 in N_2 gas ambient compared with 100% reduction achieved in air after 20 min photoreaction.
397 This can be attributed to important roles of O_2 in the photocatalytic reaction process. Besides,
398 it has been reported that $O_2^{\bullet-}$ can reduce Cr(VI) to Cr(III) [56, 57]. Thus, in this study, $O_2^{\bullet-}$ may

399 also tend to reduce Cr(VI) during the photocatalytic reaction process. However, Cr(VI) can also
400 be reduced in the absence of O_2, as illustrated in **Figure 6a**. This indicates that CB electrons
401 from rGO-2CuS also contribute to the reduction of Cr(VI). While the purging effect of N_2 on
402 phenol degradation is less obvious, suggesting that the phenol could be degraded by valence
403 band (VB) holes when photogenerated electrons were scavenged by Cr(VI) in mixed
404 Cr(VI)/phenol system. In the presence of Cr(VI), conduction band (CB) electron scavenging
405 and electron-hole separation are enhanced, increasing the rate of phenol degradation, as shown
406 in **Figure 6b**.

407 In **Figure 6a**, introduction of 1 mM EDTA-Na_2, a hole scavenger, leads to a decrease in the
408 photoreduction activity of Cr(VI). Furthermore, when the reaction process was carried out
409 under N_2 ambient, Cr(VI) reduction decreased to higher extent than in the presence of EDTA-
410 Na_2 only. This could be attributed to the decreased electron transportation of the $O_2/O_2^{\bullet-}$
411 mediated reduction in the absence of dissolved oxygen. Besides, it was previously reported that
412 Cr(VI) could be reduced by either photogenerated electrons or other active species [56, 57].
413 The $O_2^{\bullet-}$ is generated from the dissolved oxygen and photo-generated electrons of the rGO-
414 2CuS under irradiation, and could then be transformed into H_2O_2 and/or hydroxyl radical ($^{\bullet}OH$)
415 in water. Potentially, the $O_2/O_2^{\bullet-}$ mediator not only improves the electron transfer for CB to
416 Cr(VI), but also promotes the formation of $^{\bullet}OH$ from H_2O per photogenerated hole [56].

417 In this study, in the event that the CB position of a semiconductor is more negative than the
418 reduction potential of $O_2/O_2^{\bullet-}$, trapping of photogenerated electrons with molecular oxygen is
419 possible to produce $O_2^{\bullet-}$ and the photocatalytic reduction is also enhanced by effective
420 consumption of photogenerated holes in this mixed photocatalytic process [51, 56].

421 The photocatalytic activity of phenol degradation with the addition of EDTA-Na_2 was also
422 examined (**Fig. 6b**). The results revealed that when EDTA-Na_2 was introduced into the reaction
423 system, it caused a rapid deactivation of the rGO-2CuS photocatalyst and the degradation

efficiency of phenol was decreased from 100% to 56% after 20 min visible light irradiation. The result clearly indicates that the phenol degradation mainly relies on the photogenerated holes [8, 58]. It is also observed that the photodegradation efficiency in air is higher than that in ambient N_2. This can be attributed to dissolved oxygen, which promotes oxidation. However, the effect of dissolved oxygen was not so obvious in the presence of EDTA-Na_2, indicating that h^+ are the most important reactive species for phenol oxidation.

In the photocatalytic reaction, the hydroxyl radical ($^{\bullet}OH$) is considered to be the most important active group. Thus, a study of $^{\bullet}OH$ radical formation can provide a quantitative index to estimate the number of charge carriers actually implicated in phenol degradation. It is well-established that the terephthalic (TA) fluorescence method is a very sensitive technique used to detect the amount of $^{\bullet}OH$ produced and whose increase implies an improvement in photocatalytic efficiency. The method relies on the reaction of TA with $^{\bullet}OH$ to generate a fluorescent TAOH (maximum emission at ~426 nm) [36, 50]. From **Figure S15a**, the rGO-2CuS nanocomposite showed a considerably higher amount of $^{\bullet}OH$ production than CuS. This outcome is in good accordance with the results of photodegradation of phenol.

From the results of the experiments, we suggest a plausible mechanism for the photocatalytic reduction of Cr(VI) and oxidation of phenol over rGO-2CuS. Under visible light irradiation, rGO-2CuS could generate electrons and holes. Following this, the electrons in the CB of the rGO-2CuS in the ambient air are scavenged by O_2 to generate $O_2^{\bullet-}$ and migrate to Cr(VI) to reduce it. Meanwhile, the photogenerated holes left behind in the VB could produce $^{\bullet}OH$ from H_2O. H_2O_2 could be produced by superoxide radical and H^+. Besides, $O_2^{\bullet-}$ not only could induce organics oxidation, but also could promote the Cr(VI) reduction by a two-step $O_2^{\bullet-}$ mediated indirect reduction process [56]. In addition, due to the high oxidation efficiency of H_2O_2, its existence would inevitably lead to the oxidation of reduced chromium to Cr(VI). The existence of H_2O_2 in the catalytic system was highlighted by the absorption peak of o-

449 tolidine at 446 nm in the UV-vis spectrum [51, 59]. From **Figure S15b**, as the intensity of the
450 absorption peak decreases, the H_2O_2 content of the simple solution of Cr(VI) and phenol
451 decreases compared to that of the water under visible light irradiation. In case the Cr(VI)/phenol
452 combined system, almost no H_2O_2 could be observed, suggesting that phenol degradation could
453 be effective in consuming H_2O_2 and inhibiting oxidation of the lower valence states of
454 chromium to improve Cr(VI) reduction activity [51]. Moreover, the photogenerated holes and
455 various active oxidants, such as H_2O_2, $^{\bullet}OH$ and $O_2^{\bullet-}$, could oxidize phenol. During this
456 photocatalytic reaction system, Cr(VI) acts as an electron acceptor, which can react with the
457 photogenerated CB electrons; and meanwhile, phenol acts as an electron donor, which can react
458 with the photoexcited holes. Both processes can enhance the separation rate of the
459 photogenerated electron holes, resulting in much more CB electrons for Cr(VI) reduction and
460 VB holes for phenol oxidation.

461 The above results show the synergistic effect of mixed Cr(VI)/phenol system. The
462 generation of photogenerated electron-hole pairs, radicals and the reaction process can be
463 summarized according to the following equations:

$$h\nu \xrightarrow{\text{rGO-2CuS}} \text{rGO-2CuS} + (h_{VB}^{+} \rightarrow + e_{CB}^{-}) \quad (4)$$

$$O_2 + e_{CB}^{-} \rightarrow O_2^{\bullet-} \quad (5)$$

$$\text{Cr (VI)} \xrightarrow{+\,3e_{CB}^{-}} \text{Cr (III)} \quad (6)$$

$$H_2O + h_{VB}^{+} \rightarrow H^{+} + {}^{\bullet}OH \quad (7)$$

$$O_2^{\bullet-} + H^{+} \rightarrow {}^{\bullet}OOH \quad (8)$$

$$2O_2^{-} + 2H^{+} \rightarrow O_2 + H_2O_2 \quad (9)$$

$${}^{\bullet}OOH + H^{+} + e_{CB}^{-} \rightarrow H_2O_2 \quad (10)$$

$$H_2O_2 + e_{CB}^{-} \rightarrow {}^{\bullet}OH + OH^{-} \quad (11)$$

$$h_{VB}^{+} + \text{Phenol} \rightarrow \text{degradation products} \quad (12)$$

$$O_2^{\bullet-}/H_2O_2/^{\bullet}OH + \text{Phenol} \rightarrow \text{degradation products} \quad (13)$$

464

465 Therefore, based on the results and analysis of the experiments, a plausible mechanism was
466 proposed and illustrated in **Figure 7**.

467

468 **4. Conclusion**

469 In conclusion, rGO/CuS composites of different rGO/CuS weight (2/1, 1/1, 1/2) ratios were
470 fabricated *via* a facile one-step method and their photocatalytic activity in the reduction of
471 Cr(VI) was studied under visible light irradiation. The rGO-2CuS nanocomposite exhibited a
472 significantly high photocatalytic activity under visible light irradiation. In the Cr(VI)/phenol
473 mixed reaction solution, rGO-2CuS displayed enhanced photocatalytic activity for the
474 simultaneous photocatalytic reduction of Cr(VI) and oxidation of phenol. Cycling experiments
475 revealed that the prepared rGO-2CuS presents high stability. The phenol degradation, which
476 effectively consumes H_2O_2, $O_2^{\bullet-}$, $^{\bullet}OH$ and holes, not only promotes separation of
477 photogenerated electrons and holes, but also increases chromium reduction in Cr(VI)/phenol
478 systems. The detailed reaction mechanism for the photocatalytic reduction of Cr(VI) and
479 oxidation of phenol over rGO-2CuS was proposed. The highly effective photoactivity and high
480 stability properties effectively remove a large number of organic pollutants in aqueous systems,
481 which can potentially be applied in the photocatalytic field.

482

483 **Acknowledgements**

484 The authors gratefully acknowledge financial support from the Centre National de la Recherche
485 Scientifique (CNRS), the University of Lille - Sciences and Technologies, and the Hauts-de-
486 France region. Yacine Cherifi thanks the Algerian Ministry of Higher Education and Scientific
487 Research (M.E.S.R.S) for a PNE fellowship. ICP analyses were performed in the «

Spectrométrie par torche à plasma » platform of the Research Federation Michel-Eugène Chevreul hosted by the LASIRE laboratory.

References

[1] W. Liu, T. Wang, A.G.L. Borthwick, Y. Wang, X. Yin, X. Li, J. Ni, Adsorption of Pb^{2+}, Cd^{2+}, Cu^{2+} and Cr^{3+} onto titanate nanotubes: Competition and effect of inorganic ions, Sci. Total Environ., 456-457 (2013) 171-180.

[2] S. Nezar, Y. Cherifi, A. Barras, A. Addad, E. Dogheche, N. Saoula, N.A. Laoufi, P. Roussel, S. Szunerits, R. Boukherroub, Efficient reduction of Cr(VI) under visible light irradiation using CuS nanostructures, Arab. J. Chem., 12 (2019) 215-224.

[3] X. Bai, Y. Du, X. Hu, Y. He, C. He, E. Liu, J. Fan, Synergy removal of Cr (VI) and organic pollutants over RP-MoS_2/rGO photocatalyst, App. Catal. B, 239 (2018) 204-213.

[4] J.J. Testa, M.A. Grela, M.I. Litter, Heterogeneous Photocatalytic Reduction of Chromium(VI) over TiO_2 Particles in the Presence of Oxalate: Involvement of Cr(V) Species, Environ. Sci. Technol., 38 (2004) 1589-1594.

[5] B. Nanda, A.C. Pradhan, K.M. Parida, Fabrication of mesoporous CuO/ZrO_2-MCM-41 nanocomposites for photocatalytic reduction of Cr(VI), Chem. Eng. J., 316 (2017) 1122-1135.

[6] Y. Deng, T. Long, H. Zhao, L. Zhu, J. Chen, Application of porous N-methylimidazolium strongly basic anion exchange resins on Cr(VI) adsorption from electroplating wastewater, Sep. Sci. Technol., 47 (2012) 256-263.

[7] N. Abdullah, N. Yusof, W.J. Lau, J. Jaafar, A.F. Ismail, Recent trends of heavy metal removal from water/wastewater by membrane technologies, J. Ind. Eng. Chem., 76 (2019) 17-38.

[8] Y. Deng, L. Tang, G. Zeng, Z. Zhu, M. Yan, Y. Zhou, J. Wang, Y. Liu, J. Wang, Insight into highly efficient simultaneous photocatalytic removal of Cr(VI) and 2,4-diclorophenol

513 under visible light irradiation by phosphorus doped porous ultrathin g-C_3N_4 nanosheets from
514 aqueous media: Performance and reaction mechanism, Appl. Catal. B, 203 (2017) 343-354.
515 [9] S.-M. Lam, J.-C. Sin, I. Satoshi, A.Z. Abdullah, A.R. Mohamed, Enhanced sunlight
516 photocatalytic performance over Nb_2O_5/ZnO nanorod composites and the mechanism study,
517 Appl. Catal. A, 471 (2014) 126-135.
518 [10] F. Liu, J. Yu, G. Tu, L. Qu, J. Xiao, Y. Liu, L. Wang, J. Lei, J. Zhang, Carbon nitride
519 coupled Ti-SBA15 catalyst for visible-light-driven photocatalytic reduction of Cr(VI) and the
520 synergistic oxidation of phenol, Appl. Catal. B, 201 (2017) 1-11.
521 [11] S. Sajjad, S.A.K. Leghari, F. Chen, J. Zhang, Bismuth-doped ordered mesoporous TiO_2:
522 Visible-light catalyst for simultaneous degradation of phenol and chromium, Chem. Eur. J., 16
523 (2010) 13795-13804.
524 [12] X. Wang, M. Hong, F. Zhang, Z. Zhuang, Y. Yu, Recyclable nanoscale zero valent iron
525 doped g-C_3N_4/MoS_2 for efficient photocatalysis of RhB and Cr(VI) driven by visible light, ACS
526 Sustain. Chem. Eng., 4 (2016) 4055-4063.
527 [13] B. Sun, E.P. Reddy, P.G. Smirniotis, Visible Light Cr(VI) Reduction and Organic
528 Chemical Oxidation by TiO_2 Photocatalysis, Environ. Sci. Technol., 39 (2005) 6251-6259.
529 [14] L. Huang, Q. Chan, X. Wu, H. Wang, Y. Liu, The simultaneous photocatalytic degradation
530 of phenol and reduction of Cr(VI) by TiO_2/CNTs, J. Ind. Eng. Chem., 18 (2012) 574-580.
531 [15] Z. Jin, Y.-X. Zhang, F.-L. Meng, Y. Jia, T. Luo, X.-Y. Yu, J. Wang, J.-H. Liu, X.-J. Huang,
532 Facile synthesis of porous single crystalline ZnO nanoplates and their application in
533 photocatalytic reduction of Cr(VI) in the presence of phenol, J. Hazard. Mater., 276 (2014) 400-
534 407.
535 [16] L. Zhou, L. Wang, J. Lei, Y. Liu, J. Zhang, Fabrication of TiO_2/Co-g-C_3N_4 heterojunction
536 catalyst and its photocatalytic performance, Catal. Commun., 89 (2017) 125-128.

537 [17] D. Lu, M. Yang, P. Fang, C. Li, L. Jiang, Enhanced photocatalytic degradation of aqueous
538 phenol and Cr(VI) over visible-light-driven Tb_xO_y loaded TiO_2-oriented nanosheets, Appl.
539 Surf. Sci., 399 (2017) 167-184.
540 [18] J. Zhang, Y. Li, L. Li, W. Li, C. Yang, Dual functional N‑ doped TiO_2‑ carbon composite
541 fibers for efficient removal of water pollutants, ACS Sustainable Chem. Eng., 6 (2018)
542 12893−12905.
543 [19] X. Zhang, Y. Chen, Q. Shang, Y. Guo, Copper doping and organic sensitization enhance
544 photocatalytic activity of titanium dioxide: Efficient degradation of phenol and
545 tetrabromobisphenol A, Sci. Total Environm., 716 (2020) 137144.
546 [20] Y. Deng, Y. Xiao, Y. Zhou, T. Zeng, M. Xing, J. Zhang, A structural engineering-inspired
547 CdS based composite for photocatalytic remediation of organic pollutant and hexavalent
548 chromium, Catal. Today 335 (2019) 101-109.
549 [21] B. Xie, H. Zhang, P. Cai, R. Qiu, Y. Xiong, Simultaneous photocatalytic reduction of
550 Cr(VI) and oxidation of phenol over monoclinic $BiVO_4$ under visible light irradiation,
551 Chemosphere, 63 (2006) 956-963.
552 [22] A. Chen, Z. Bian, J. Xu, X. Xin, H. Wang, Simultaneous removal of Cr(VI) and phenol
553 contaminants using Z-scheme bismuth oxyiodide/reduced graphene oxide/bismuth sulfide
554 system under visible-light irradiation, Chemosphere, 188 (2017) 659-666.
555 [23] S. Patnaik, K.K. Das, A. Mohanty, K. Parida, Enhanced photo catalytic reduction of Cr
556 (VI) over polymer-sensitized g-C_3N_4/$ZnFe_2O_4$ and its synergism with phenol oxidation under
557 visible light irradiation, Catal. Today, 315 (2018) 52-66.
558 [24] Q. Wang, C. Zhang, H. Wu, Q. Gao, R. Duan, C. Chen, Fabrication of b-phase AgI and
559 Bi_2O_3 co-decorated $Bi_2O_2CO_3$ heterojunctions with enhanced photocatalytic performance, J.
560 Colloid Interface Sci., 547 (2019) 1-13.

561 [25] S. Patnaik, D.P. Sahoo, K.M. Parida, Bimetallic co-effect of Au-Pd alloyed nanoparticles
562 on mesoporous silica modified g-C_3N_4 for single and simultaneous photocatalytic oxidation of
563 phenol and reduction of hexavalent chromium, J. Colloid Interface Sci., 560 (2020) 519-535.
564 [26] S. Goel, F. Chen, W. Cai, Synthesis and biomedical applications of copper sulfide
565 nanoparticles: From sensors to theranostics, Small, 10 (2014) 631-645.
566 [27] W. van der Stam, A.C. Berends, C. de Mello Donega, Prospects of Colloidal Copper
567 Chalcogenide Nanocrystals, ChemPhysChem, 17 (2016) 559-581.
568 [28] Y. Zhao, C. Burda, Development of plasmonic semiconductor nanomaterials with copper
569 chalcogenides for a future with sustainable energy materials, Energy Environ. Sci., 5 (2012)
570 5564-5576.
571 [29] A.C. Estrada, F.M. Silva, S.F. Soares, J.A.P. Coutinho, T. Trindade, An ionic liquid route
572 to prepare copper sulphide nanocrystals aiming at photocatalytic applications, RSC Adv., 6
573 (2016) 34521-34528.
574 [30] G. Nie, L. Zhang, X. Lu, X. Bian, W. Sun, C. Wang, A one-pot and in situ synthesis of
575 CuS-graphene nanosheet composites with enhanced peroxidase-like catalytic activity, Dalton
576 Trans., 42 (2013) 14006-14013.
577 [31] X. Zhao, F. Zhang, D. Lu, Y. Du, W. Ye, C. Wang, Fabrication of a CuS/graphene
578 nanocomposite modified electrode and its application for electrochemical determination of
579 esculetin, Anal. Methods, 5 (2013) 3992-3998.
580 [32] L. Ye, J. Fu, Z. Xu, R. Yuan, Z. Li, Facile one-pot solvothermal method to synthesize
581 sheet-on-sheet reduced graphene oxide (RGO)/$ZnIn_2S_4$ nanocomposites with superior
582 photocatalytic performance, ACS Appl. Mater. Interfaces, 6 (2014) 3483-3490.
583 [33] E. Kusiak-Nejman, A. Wanag, Ł. Kowalczyk, J. Kapica-Kozar, C. Colbeau-Justin, M.G.
584 Mendez Medrano, A.W. Morawski, Graphene oxide-TiO_2 and reduced graphene oxide-TiO_2

585 nanocomposites: Insight in charge-carrier lifetime measurements, Catal. Today, 287 (2017)
586 189-195.
587 [34] X.-S. Hu, Y. Shen, Y.-T. Zhang, H.-F. Zhang, L.-H. Xu, Y.-J. Xing, Synthesis of flower-
588 like CuS/reduced graphene oxide (RGO) composites with significantly enhanced photocatalytic
589 performance, J. Alloys Compds., 695 (2017) 1778-1785.
590 [35] C. Ding, D. Su, W. Ma, Y. Zhao, D. Yan, J. Li, H. Jin, Design of hierarchical CuS/graphene
591 architectures with enhanced lithium storage capability, Appl. Surf. Sci., 403 (2017) 1-8.
592 [36] T. Hirakawa, Y. Nosaka, Properties of $O_2^{\bullet-}$ and $OH^{\bullet}$ formed in TiO_2 aqueous suspensions
593 by photocatalytic reaction and the influence of H_2O_2 and some ions, Langmuir, 18 (2002) 3247-
594 3254.
595 [37] A. Swaidan, A. Barras, A. Addad, J.-F. Tahon, J. Toufaily, T. Hamieh, S. Szunerits, R.
596 Boukherroub, Colorimetric sensing of dopamine in beef meat using copper sulfide encapsulated
597 within bovine serum albumin functionalized with copper phosphate (CuS-BSA-$Cu_3(PO4)_2$)
598 nanoparticles, J. Colloid Interface Sci., 582 (2021) 732-740.
599 [38] M. Saranya, R. Ramachandran, P. Kollu, S.K. Jeong, A.N. Grace, A template-free facile
600 approach for the synthesis of CuS–rGO nanocomposites towards enhanced photocatalytic
601 reduction of organic contaminants and textile effluents, RSC Adv., 5 (2015) 15831-15840.
602 [39] Y. Cherifi, A. Addad, H. Vezin, A. Barras, B. Ouddane, A. Chaouchi, S. Szunerits, R.
603 Boukherroub, PMS activation using reduced graphene oxide under sonication: Efficient metal-
604 free catalytic system for the degradation of rhodamine B, bisphenol A, and tetracycline,
605 Ultrason. Sonochem., 52 (2019) 164-175.
606 [40] S. Stankovich, D.A. Dikin, R.D. Piner, K.A. Kohlhaas, A. Kleinhammes, Y. Jia, Y. Wu,
607 S.T. Nguyen, R.S. Ruoff, Synthesis of graphene-based nanosheets via chemical reduction of
608 exfoliated graphite oxide, Carbon, 45 (2007) 1558-1565.

[41] Z. Zhan, C. Liu, L. Zheng, G. Sun, B. Li, Q. Zhang, Photoresponse of multi-walled carbon nanotube–copper sulfide (MWNT–CuS) hybrid nanostructures, Phys. Chem. Chem. Phys., 13 (2011) 20471-20475.

[42] Y. Zhang, J. Tian, H. Li, L. Wang, X. Qin, A.M. Asiri, A.O. Al-Youbi, X. Sun, Biomolecule-Assisted, Environmentally Friendly, One-Pot Synthesis of CuS/Reduced Graphene Oxide Nanocomposites with Enhanced Photocatalytic Performance, Langmuir, 28 (2012) 12893-12900.

[43] N. Karikalan, R. Karthik, S.-M. Chen, C. Karuppiah, A. Elangovan, Sonochemical synthesis of sulfur doped reduced graphene oxide supported CuS nanoparticles for the non-enzymatic glucose sensor applications, Sci. Rep., 7 (2017) 2494.

[44] J. Ghijsen, L.H. Tjeng, J. van Elp, H. Eskes, J. Westerink, G.A. Sawatzky, M.T. Czyzyk, Electronic structure of Cu_2O and CuO, Phys. Rev. B, 38 (1988) 11322-11330.

[45] D. Yuan, G. Huang, F. Zhang, D. Yin, L. Wang, Facile synthesis of CuS/rGO composite with enhanced electrochemical lithium-storage properties through microwave-assisted hydrothermal method, Electrochim. Acta, 203 (2016) 238-245.

[46] Y. Zhao, H. Pan, Y. Lou, X. Qiu, J. Zhu, C. Burda, Plasmonic $Cu_{2-x}S$ Nanocrystals: Optical and Structural Properties of Copper-Deficient Copper(I) Sulfides, J. Am. Chem. Soc., 131 (2009) 4253-4261.

[47] J.S. Lee, K.H. You, C.B. Park, Highly photoactive, low bandgap TiO_2 nanoparticles wrapped by graphene, Adv. Mater., 24 (2012) 1084-1088.

[48] J. Muñoz, X. Domènech, TiO_2 catalysed reduction of Cr(VI) in aqueous solutions under ultraviolet illumination, J. Appl. Electrochem., 20 (1990) 518-521.

[49] Q. Wu, J. Zhao, G. Qin, C. Wang, X. Tong, S. Xue, Photocatalytic reduction of Cr(VI) with TiO_2 film under visible light, Appl. Catal. B, 142-143 (2013) 142-148.

633 [50] D. Lu, W. Chai, M. Yang, P. Fang, W. Wu, B. Zhao, R. Xiong, H. Wang, Visible light
634 induced photocatalytic removal of Cr(VI) over TiO_2-based nanosheets loaded with surface-
635 enriched CoOx nanoparticles and its synergism with phenol oxidation, Appl. Catal. B, 190
636 (2016) 44-65.
637 [51] J.-C. Wang, J. Ren, H.-C. Yao, L. Zhang, J.-S. Wang, S.-Q. Zang, L.-F. Han, Z.-J. Li,
638 Synergistic photocatalysis of Cr(VI) reduction and 4-chlorophenol degradation over
639 hydroxylated α-Fe_2O_3 under visible light irradiation, J. Hazard. Mater., 311 (2016) 11-19.
640 [52] V.A. Peyman, S. Azizian, A sharp jump in photocatalytic activity of elemental sulfur for
641 dye degradation in alkaline solution, Photochem. Photobiol., (2020. DOI: 10.1111/php.13301).
642 [53] J. Burés, A simple graphical method to determine the order in catalyst, Angew. Chem. Int.
643 Ed., 55 (2016) 2028-2031.
644 [54] R. Vinu, G. Madras, Kinetics of simultaneous photocatalytic degradation of phenolic
645 compounds and reduction of Metal Ions with nano-TiO_2, Environ. Sci. Technol., 42 (2008) 913-
646 919.
647 [55] Y. Tadjenant, N. Dokhan, A. Barras, A. Addad, R. Jijie, S. Szunerits, R. Boukherroub,
648 Graphene oxide chemically reduced and functionalized with KOH-PEI for efficient Cr(VI)
649 adsorption and reduction in acidic medium, Chemosphere, 258 (2020) 127316.
650 [56] G. Dong, L. Zhang, Synthesis and enhanced Cr(VI) photoreduction property of formate
651 anion containing graphitic carbon nitride, J. Phys. Chem. C, 117 (2013) 4062-4068.
652 [57] X. Hu, H. Ji, F. Chang, Y. Luo, Simultaneous photocatalytic Cr(VI) reduction and 2,4,6-
653 TCP oxidation over g-C_3N_4 under visible light irradiation, Catal. Today, 224 (2014) 34-40.
654 [58] X. Chen, Y. Dai, J. Guo, T. Liu, X. Wang, Novel magnetically separable reduced graphene
655 oxide (RGO)/$ZnFe_2O_4$/Ag_3PO_4 nanocomposites for enhanced photocatalytic performance
656 toward 2,4-dichlorophenol under visible light, Ind. Eng. Chem. Res., 55 (2016) 568-578.

[59] J. Liu, Y. Liu, N. Liu, Y. Han, X. Zhang, H. Huang, Y. Lifshitz, S.-T. Lee, J. Zhong, Z. Kang, Metal-free efficient photocatalyst for stable visible water splitting via a two-electron pathway, Science, 347 (2015) 970-974.

682 **Figure captions**

683 **Figure 1**: X-ray diffraction patterns of pure CuS and rGO-2CuS nanocomposite.

684 **Figure 2:** (a) Typical TEM images, (b) HRTEM image (inset is the high magnification TEM
685 image of rGO-2CuS), (c) HRTEM image showing lattice planes, and (d) selected area electron
686 diffraction (SAED) pattern of rGO-2CuS.

687 **Figure 3:** Photocatalytic reduction of Cr(VI) (20 mg/L) over rGO-CuS (0.5 g/L) under visible
688 light irradiation ($\lambda > 420$ nm).

689 **Figure 4:** (**a**) Photocatalytic reduction efficiencies of Cr(VI) (20 mg/L) in presence and absence
690 of phenol (10 mg/L) at different ratios, (blank test: reduction of Cr(VI) in presence of phenol
691 (ratio 1:2) without catalyst). (**b**) Photocatalytic degradation of phenol (20 mg/L) in presence
692 and absence of Cr(VI) (10 mg/L) at different ratios, (blank test: degradation of phenol in
693 presence of Cr(VI) (ratio 1:2) without catalyst); rGO-2CuS=0.5 g/L, pH = 5.8, visible light.

694 **Figure 5:** (**a**) Efficiency of removal of Cr, Cr(VI)+Cr(III) in the coexisting Cr(VI)-phenol
695 system, (b) Distribution of the intermediates during the degradation process of phenol.

696 **Figure 6:** (**a**) Cr(VI) reduction and (**b**) phenol degradation in presence of different scavengers
697 and various ambient conditions under visible light irradiation. Reaction conditions: catalyst
698 loading = 0.5 g/L, [phenol]=20 mg/L, [Cr(VI)]=20 mg/L, pH= 5.8, T = 25°C.

699 **Figure 7:** Schematic illustration for the synergistic photocatalysis of Cr(VI) reduction and
700 phenol degradation over rGO-2CuS catalyst.

701

702

703

704

705

706

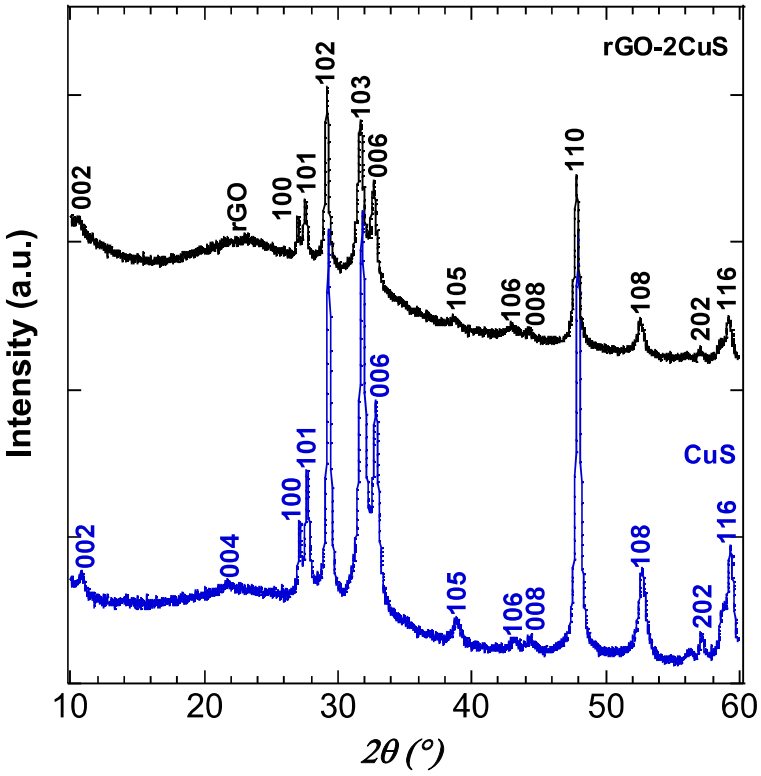
rGO-2CuS
CuS
Intensity (a.u.)
2θ (°)
10
20
30
40
50
60
002
rGO
100
101
102
103
006
105
106
008
110
108
202
116
002
004
100
101
006
105
106
008
108
202
116

Figure 1

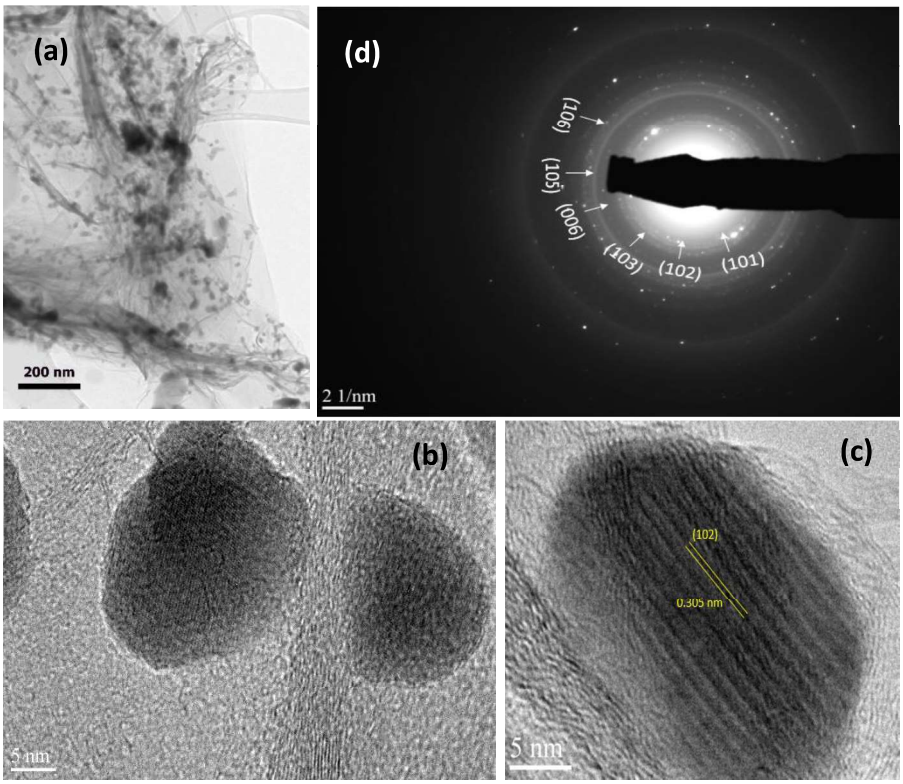

Figure 2

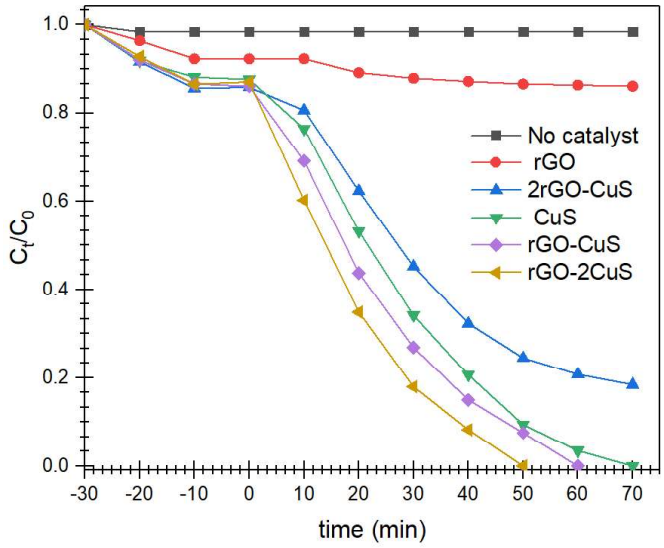
1.0
0.8
0.6
0.4
0.2
0.0
C_t/C_0
-30
-20
-10
0
10
20
30
40
50
60
70
time (min)
No catalyst
rGO
2rGO-CuS
CuS
rGO-CuS
rGO-2CuS

Figure 3

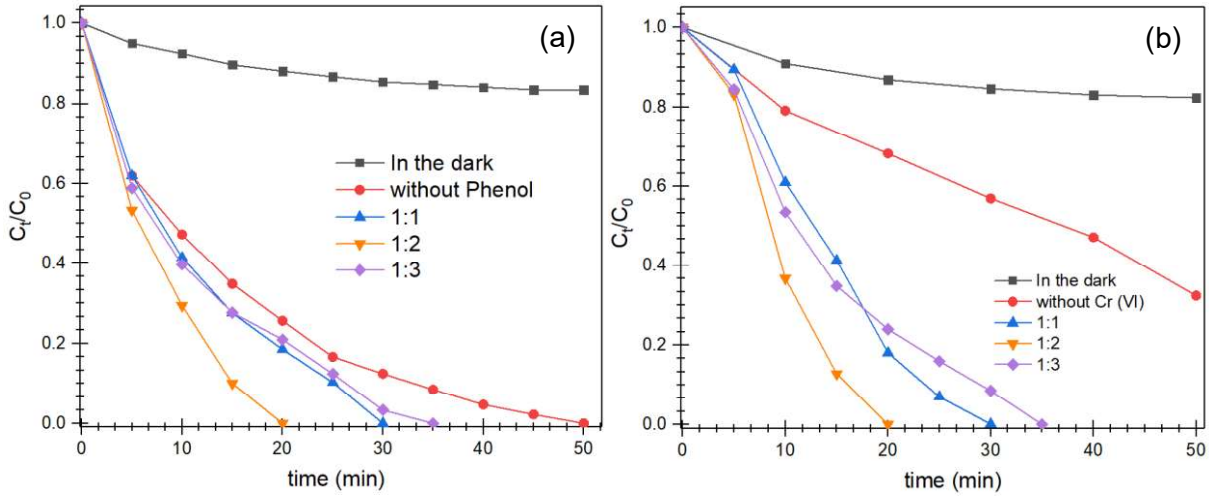
(a)
In the dark
without Phenol
1:1
1:2
1:3
C_t/C_0
time (min)
(b)
In the dark
without Cr (VI)
1:1
1:2
1:3
C_t/C_0
time (min)

Figure 4

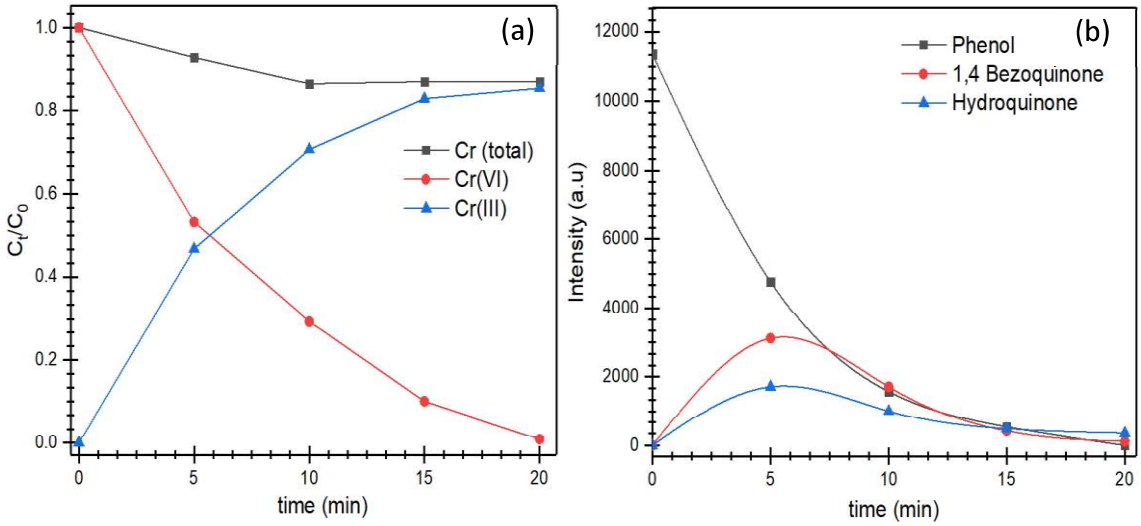
(a)
1.0
0.8
0.6
0.4
0.2
0.0
C_t/C_0
Cr (total)
Cr(VI)
Cr(III)
0
5
10
15
20
time (min)
(b)
12000
10000
8000
6000
4000
2000
0
Intensity (a.u)
Phenol
1,4 Bezoquinone
Hydroquinone
0
5
10
15
20
time (min)

Figure 5

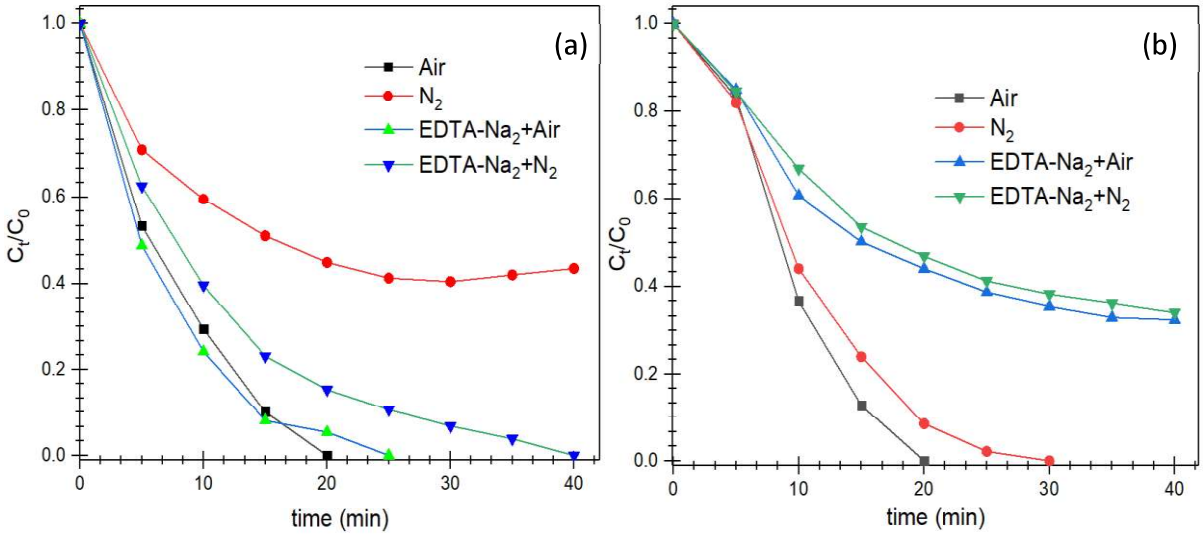
(a)
Air
N2
EDTA-Na2+Air
EDTA-Na2+N2
Ct/C0
time (min)
(b)
Air
N2
EDTA-Na2+Air
EDTA-Na2+N2
Ct/C0
time (min)

Figure 6

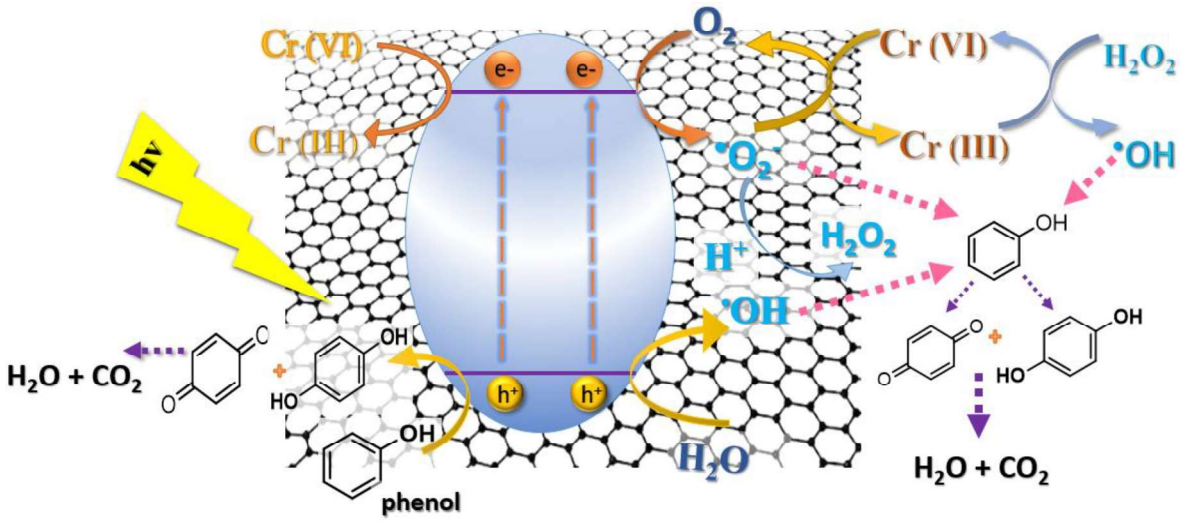
Cr (VI)
Cr (III)
hv
e-
e-
h+
h+
O2
Cr (VI)
Cr (III)
H2O2
•OH
•O2-
H2O2
H+
•OH
H2O
H2O + CO2
phenol
H2O + CO2

Figure 7